UNIVERSITY OF CALIFORNIA SAN DIEGO

Ranking Inverse Kinematic Solutions for the Control of a CT-compatible Robotic Platform

A Thesis submitted in partial satisfaction of the requirements
for the degree of Master of Science

in

Electrical Engineering (Intelligent Systems, Robotics, and Control)

by

Taylor West Henderson

Committee in charge:

Professor Michael Yip, Chair
Professor Nikolay Atanasov
Professor Alexander Norbash

2020

The Thesis of Taylor West Henderson is approved, and it is acceptable in quality and form for publication on microfilm and electronically:

Chair

University of California San Diego

2020

DEDICATION

To my husband Daniel, whom has inspired and comforted me in this journey.

To my parents, Trina and Jay, and my sister Laine for their love and strength, and for pushing me to always follow my dreams.

To my family, friends, professors, and mentors for their encouragement and support.

TABLE OF CONTENTS

Signature Page iii

Dedication iv

Table of Contents v

List of Figures vii

List of Tables viii

Acknowledgements ix

Abstract of the Thesis x

Chapter 1 Introduction 1
1.1 Lung Biopsy Overview 1
1.2 Robots for Lung Biopsy: Previous Work 2
1.3 CRANE: CT Robotic Arm and Needle Emplacer 3
1.4 Our Goal: Ranked Options for Robot Configurations 5

Chapter 2 System Overview and Simulation 6
2.1 System Overview 6
2.1.1 CRANE Design 6
2.1.2 Current and Proposed Clinical Workflow 7
2.2 Simulations 8
2.2.1 PyRep and CoppeliaSim 8
2.2.2 Workspace Evaluation 10

Chapter 3 Obtaining Inverse Kinematics Solutions 12
3.1 Preliminaries 12
3.2 Damped Least Squares (DLS) Method 14
3.3 Task Augmentation 15
3.3.1 Obstacle Avoidance 16
3.3.2 Limited Joint Range 18
3.3.3 Overall Solution 19
3.4 Randomized Search to Obtain Multiple “Unique” IK Solutions 20

Chapter 4 Cone Maneuverability 22

Chapter 5 Ranking IK Solutions and Planning 26
5.1 Additional Metrics 26
5.1.1 Joint Limit Avoidance 26
5.1.2 Distance to Collision 27
5.1.3 Distance to Singularities 28

5.2 Weighting Scores 29
5.3 Path Planning 29

Chapter 6 Experimental Results 32
6.1 Evaluation of Chosen Metrics 32
6.2 Weighting Scores Across Needle Orientations 33
6.3 End-to-End Control Scheme 36

Chapter 7 Conclusion 41
7.1 Discussion and Future Work 41
7.2 Summary 42

Bibliography 44

LIST OF FIGURES

Figure 2.1. CRANE with serial-link redundant 8-DoF arm. A) back-end positioning stage, B) remote 4-DoF arm and clutching needle driver 7

Figure 2.2. Needle biopsy simulation environment. A) a full CAD model of the CRANE robot, B) CT bore, and C) a human body model. 9

Figure 2.3. The reachable workspace for target poses with a) 160°, b) 180°, and c) 200° α angles. 11

Figure 4.1. Depiction of conical movement of biopsy needle for maneuverability metric. 23

Figure 4.2. Example of a a) complete and b) incomplete cone movement of the CRANE needle. The brown orb at the end of the arm represents the needle tip end-effector. The pink curve in a) represents the movement of the needle end around the cone surface, with a starting position in the center of the circle. 25

Figure 5.1. Example of a) an IK setup configuration and b) corresponding path generated using RRT* algorithm. The brown orb at the end of the arm represents the needle tip end-effector. The pink curve represents the end-effector path to the desired joint configuration and target needle pose. 31

Figure 6.1. Scores for each configuration metric including: 1) all scores across all targets, 2) average scores across all targets, and 3) spread of scores across targets. Approximately 1000 targets are sampled on the anterior surface of the body model with target vectors perpendicular to the CT bed. 34

Figure 6.1. Scores for each configuration metric including: a) all scores across all targets, b) average scores across all targets, and c) spread of scores across targets. Approximately 1000 targets are sampled on the anterior surface of the body model with target vectors perpendicular to the CT bed, Continued. 35

Figure 6.2. Average weighted scores across targets on the human body model at various needle orientations and weighting combinations. Each row of the subfigure grid corresponds to a different weighting combination, while each column corresponds to a different needle orientation. 37

Figure 6.3. Highest ranked configuration for a given target with various metric weighting combinations. 38

Figure 6.4. The average weighted configuration scores for a single target on the anterior surface of the chest at various needle α-orientations. 180° corresponds to the negative z-axis of the needle aligned perpendicular to the CT bed, representing a 90° rotation from the original needle z-axis orientation. . . . 39

LIST OF TABLES

Table 6.1. Speed of execution for calculations of interest and entirety of end-to-end control scheme. The full algorithm used for these calculations samples up to 10 valid configurations per target. 39

ACKNOWLEDGEMENTS

I would like to acknowledge Professor Michael Yip for his support and encouragement in this project and for allowing so many opportunities for me to grow and excel as a researcher. All of the work presented in this thesis won't be possible without his patience and guidance.

I would like to thank Dimitri Schrieber for constantly answering my questions, giving direction when I was stuck, and supporting me in achieving this project. Without his help and his robot, this research could not have been achieved.

I would like to also acknowledge my past and present lab mates in the Advanced Robotics and Control Lab (ARCLab) who have supported me with a mix of academic discussion and delightful conversation.

ABSTRACT OF THE THESIS

Ranking Inverse Kinematic Solutions for the Control of a CT-compatible Robotic Platform

by

Taylor West Henderson

Master of Science in Electrical Engineering (Intelligent Systems, Robotics, and Control)

University of California San Diego, 2020

Professor Michael Yip, Chair

Robotic systems have been widely employed for many needle biopsy applications, such as transthoracic lung biopsies that enable early diagnosis of primary lung cancers with small, distal lesions. The CRANE robot, a robotic needle positioning system for CT guided procedures, is one such system that has demonstrated a low-profile, high dexterity, and a large number of degrees of freedom. In this thesis, we present an end-to-end automated control scheme for the CRANE robotic platform that optimizes a robotic configuration over several defined metrics relevant to the successful completion of a transthoracic needle biopsy procedure. For a given needle tip target pose, multiple viable arm configurations are generated and ranked based several metric criteria. Once a configuration is chosen, a planner is run to find a collision-free path from

the robot's initial position outside of the CT-bore to this final configuration within the bore.

Chapter 1

Introduction

1.1 Lung Biopsy Overview

For many years, primary lung cancer has remained the leading cause of cancer-related death in both men and women worldwide, with only a 17% five-year survival rate after the appearance of related symptoms [1]. Respiratory and other physicians play a pivotal role in performing initial evaluations for patients with suspected lung cancer, with one of their key goals being the collection of an early tissue diagnosis. Over the past 20 years, the complexity of this task has grown with the changes in precision and efficacy of lung cancer treatments, the epidemiology of lung cancer, and the tools available for obtaining a tissue diagnosis [2].

In large central lesions, tissue sampling with traditional bronchoscopy methods have a high diagnostic yield of approximately 88%. This sensitivity declines significantly, however, as lesions decrease in size and become more distal [3], with one study giving diagnostic yields as low as 14% for lesions less than 2cm in size and located in the outer third of the lung [4].

As a result, radiologically guided transthoracic needle biopsy is increasingly being employed for the diagnosis of lung cancer, with published studies suggesting a diagnostic yield of about 90% in peripheral lesions [5]. However, lesion size also adversely affects the sensitivity of transthoracic needle biopsies, and the yield of these hand-guided biopsies reduces significantly in lesions under 1cm in size [6].

Additionally, there are associated complications with a transthoracic needle biopsy. To

pinpoint and subsequently sample a pulmonary lesion several centimeters below the surface of the skin, the radiologist must alternate between placing the patient in a CT scanner to view the position of the nodule and needle, and moving them out of the scanner to manually advance the needle. The lack of real-time scans and frequent, manual adjustments often lead to the necessitation of multiple punctures [7]. Rates of pneumothorax (collapsed lung) have been reported as high as 60% [8], with the risk of complication increasing as the lesions become smaller and deeper, as well as with patients who are older, current smokers and those with emphysema [9],[10]. Because this biopsy method is hand-guided, there is only a small range of angles in which the needle can be stepped with confidence, restricting the likelihood of reaching lesions that require an atypical approach to avoid sensitive nerves, vessels or bone. Finally, there is also a risk of secondary imaging-induced cancer due to repetitive CT scans. These limitations and risks have driven recent developments in techniques to more safely and efficiently localize and sample peripheral lung cancers, namely, in the realm of robotics [11].

1.2 Robots for Lung Biopsy: Previous Work

Many robotic systems have been designed for needle biopsy applications, but only a select few have been developed with the specific challenges of performing lung biopsies in mind [11],[12],[13],[14],[15],[16],[17],[18],[19]. These robotic lung biopsy approaches can be generally categorized based on their physical approach to lesions, mechanical stiffness, number of active joints, and controllers.

While these CT-compatible systems have shown successes illustrating the utility of CT-guided needle biopsy robots as a whole, each comes with its own limitations. Systems that secure to the patient's chest have better precision for positioning instruments as the body shifts but have a limited reach [20],[21]. Those with passive setup joints for transthoracic biopsy may be well suited for smaller anatomies with single approach vectors but have a restricted active range of motion [15],[22]. Platforms that utilize industrial robot arms have increased dexterity but can achieve

only a few feasible biopsy approaches as their size limits their reach into the bore [15],[19]. Other robotic systems bypass the transthoracic risks by offering a bronchoscopic approach via intraluminal steerable needles, but unfortunately have low diagnostic yield in peripheral lungs and for lesions smaller than 20mm [23],[24],[25],[26],[27],[28],[29],[30],[31],[32],[33].

When developing these robotic platforms, the specific clinical requirements for a lung biopsy must be considered. The biopsy needle at the end of the system should be able to hit 10mm biopsy targets with an average needle placement depth of 73mm [34]. Commonly used biopsy needles have a length ranging between 8cm and 30cm, and the average human lung is 10-15cm in width and 25-35cm in length. Both rib bones and vasculature prevent certain approaches, while other approaches have a high risk of puncture to the heart or diaphragm. This motivates a highly dexterous robot with a large working volume and radiolucent properties that minimize visual artifacts in the CT images.

The challenges faced when performing these precise needle biopsies, such as the compact working conditions and severe material limitations, are extremely difficult to overcome. Each of these existing robot systems have specific deficiencies in their reachable collision-free workspace and operating area, which prevent them from being used in general purpose applications. However, the recent design of CRANE (CT Robotic Arm and Needle Emplacer), a highly dexterous, low-profile, 8 degree-of-freedom (DoF) robotic arm for interventional radiology (IR) procedures overcomes several of these challenges by utilizing both high-stiffness industrial robot arm methods and low-stiffness intra-bronchoscopic needle approaches [35],[36].

1.3 CRANE: CT Robotic Arm and Needle Emplacer

This new robotic system for intra-bore radiologically guided needle interventions leverages a redundant serial linkage design. With 8-DoF cable-driven control that minimizes backlash and ensures smooth positioning and insertion of biopsy needles, CRANE's robot arm allows for numerous approach vectors to peripheral tissue targets. The robot has a large working volume and

can move and sweep through the entire CT bore. This system enables fast nodule localization and precise adjustments to the needle's trajectory for biopsy. This reduces the number of punctures and scans needed for a needle-biopsy procedure and the likelihood of some of the associated risks.

Up until recently, the CRANE robotic platform was fully remotely controlled (teleoperated) by the radiologist. Teleoperation enables direct "surgeon in-the-loop control," where the radiologist can compensate for small initial placement errors and needle deflections that occur due to tissue non-homogeneity. While this type of control method makes sense for needle movement directly into and within the tissue, it can raise some issues when the robot arm is moving within the CT bore and setting the needle's initial placement for biopsy. For those not intricately familiar with its design, this seven-jointed arm can be unintuitive to control over large distances and in a tightly confined space. If only the end-effector is controlled, it can result in sub-optimal joint configurations of the arm within the bore and limit the adjustability of the needle during the biopsy procedure.

In parallel with this thesis, early steps have been taken to automate the movement of the robot arm from its initial position to its target position above the surface of the body. Given a single target pose specified by the radiologist, a joint configuration is found via inverse kinematics and a collision-free path to that configuration is executed. However, this process stops short of evaluating the chosen configuration for its ability to facilitate the rest of the biopsy procedure. The radiologist must teleoperate the remainder of the procedure in simulation to determine whether or not the given configuration will allow for a successful biopsy. If not, a new configuration must be generated and the process repeated. Only with a successful full procedure in simulation can the CRANE be physically moved into position and the actual procedure executed.

1.4 Our Goal: Ranked Options for Robot Configurations

Thus, we present an end-to-end control scheme for this robotic platform which finds multiple arm configurations for transthoracic needle insertion and plans a feasible collision-free path to the optimal configuration from its initial position. These optimal configurations are generated based on several ranking metrics. For a given needle tip target pose, multiple viable arm configurations are generated and then ranked based on how well they meet the metric criteria. This allows the radiologist to choose among multiple options for an arm configuration for a given target needle pose based on their specific needs, and also allows them to effectively compare the feasibility and optimality of several potential entry points to a tissue nodule. Given a chosen configuration, a planner is then run to find a collision-free path from the robot's initial position outside of the CT-bore to this final configuration within the bore. The robot is subsequently moved, and the biopsy procedure can be directly and immediately performed.

Chapter 2

System Overview and Simulation

Our ranked control scheme has been implemented in CoppeliaSim (a robot simulator developed by Coppelia Robotics formerly known as V-REP) through the PyRep toolkit on an HP Z8 G4 Workstation running at 2.2 GHz. Section 2.1 will give an overview of the chosen system and its initialization, while Section 2.2 gives an overview of the simulator.

2.1 System Overview

2.1.1 CRANE Design

The 8 DoF system is composed of two distinct structures: a 4 DoF intra-bore structure with needle driving clutches and a 4 DoF exo-bore structure (Figure 2.1). The intra-bore structure's serial-link arm is cable-driven by motors located on the exo-bore structure. The mechanical benefits of this system include:

1. low gear ratio motors for faster motion and inherent safety via torque-sensing,
2. small intra-bore link lengths (7cm) and large joint ranges of motion for improved dexterity,
3. incorporation of joint mounted high resolution absolute magnetic encoders for improved system state tracking,
4. a novel clutch mechanism using Shape Memory Alloy (SMA) actuators that are helicaly wrapped around a flexure, allowing infinite depth needle insertion and retraction with a

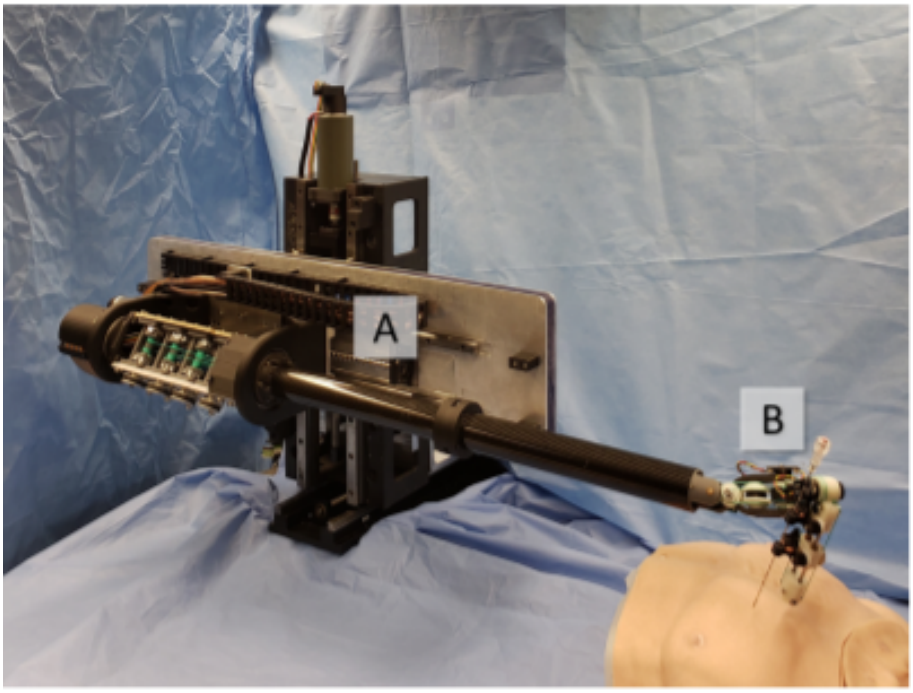

Figure 2.1. CRANE with serial-link redundant 8-DoF arm. A) back-end positioning stage, B) remote 4-DoF arm and clutching needle driver

short insertion stage.

In addition, the exo-bore backend is composed of a revolute axis on the trunnion and an X-Y-Z cartesian stage driven by ballscrew actuators, which allows for incredibly precise and accurate motions.

2.1.2 Current and Proposed Clinical Workflow

The system's current clinical workflow is as follows:

1. The robot-to-scanner calibration transform is calculated using preliminary CT scans.
2. The physician manipulates the needle into the desired setup pose. Once this setup pose is confirmed, the robot configuration is generated.
3. A collision-free path from the initial configuration to the generated configuration is found and executed in simulation.

4. The physician performs the biopsy procedure in simulation to verify that the setup configuration will lead to a successful needle biopsy.

5. Following physician confirmation, the robot follows this trajectory to the setup pose.

6. The physician iterates between simulated needle motions, robot teleoperation, and CT confirmation scans until the target is reached.

We propose, however, to vastly improve upon this workflow by optimizing the proposed joint configurations according to various metric criteria and allowing for the direct comparison of configurations generated from samples across the body. This gives the radiologist options not only in the choice of configuration for a give target pose based on their criteria, but also in the choice of target entry pose to reach a particular tissue sample. The proposed workflow is thus:

1. The robot-to-scanner calibration transform is calculated using preliminary CT scans.

2. Using the scans, the physician indicates a potential needle pose(s) for the biopsy procedure.

3. Multiple randomly seeded robot configurations are generated for this pose(s) and each is given a score based on joint limits, collision distance, maneuverability, etc (more on this in Chapters 4 and 5).

4. A collision-free path from the inital configuration to the highest scoring setup configuration (and corresponding target if applicable) is found and executed.

5. The physician proceeds with the teleoperated needle biopsy procedure.

2.2 Simulations

2.2.1 PyRep and CoppeliaSim

To conduct experiments and run simulations, we utilize CoppeliaSim, a virtual robotics experimentation platform from Coppelia Robotics formerly known as V-REP [37]. Our two main reasons for choosing this platform are:

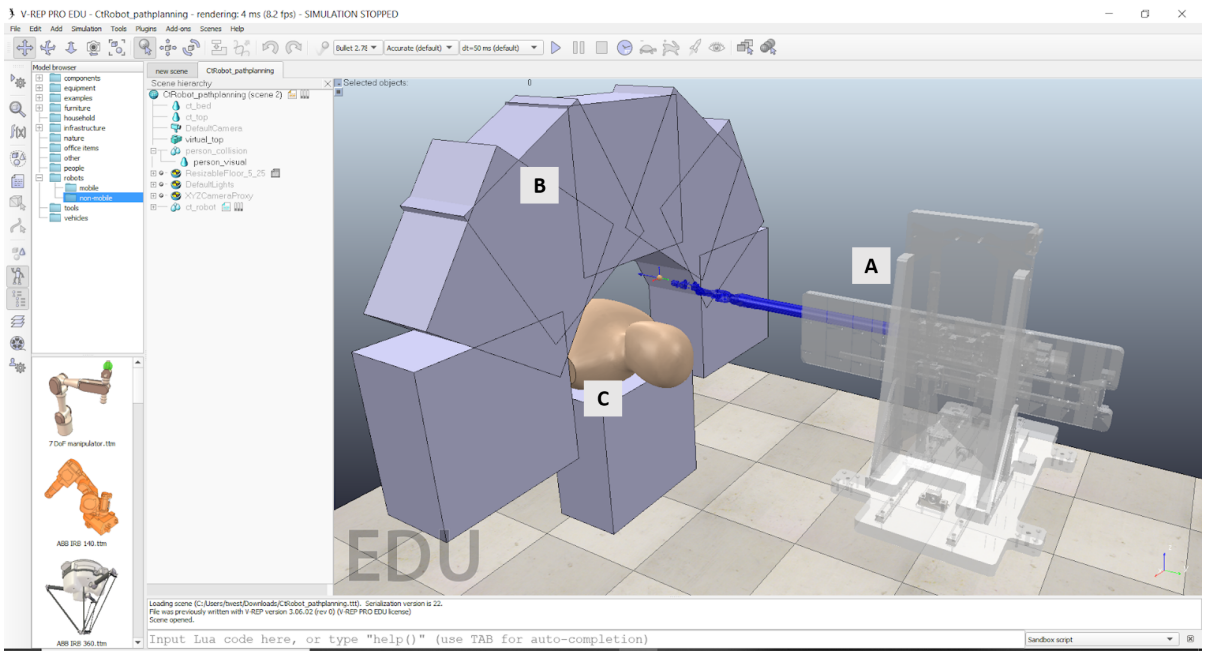

Figure 2.2. Needle biopsy simulation environment. A) a full CAD model of the CRANE robot, B) CT bore, and C) a human body model.

1. **Collision-checker:** CoppeliaSim has an embedded collision checker for fast interference checking between any mesh, octree, point cloud, or collection of those.

2. **Physics engine:** CoppeliaSim allows one to run both kinematic (i.e., with no physics engine running) and dynamic playbacks of planned motions.

With inverse and forward kinematics as well as a motion planning library, CoppeliaSim allows for the construction of an accurate and dynamic simulator that is capable of generating real-time control data for the physical robot system. To run CoppeliaSim externally from Python, we utilize PyRep [38]: a toolkit for robot learning research built on top of CoppeliaSim.

Our virtual environment contains a 65cm CT bore, a human dummy model, and a CAD model of the robot (Figure 2.2). The base of the robotic system is placed approximately 50cm superior to the patient's head outside of the CT bore, with the robot arm positioned directly into the center of the bore parallel to the CT bed. This initial position and configuration remain consistent in each of the simulations and experiments presented in this work.

2.2.2 Workspace Evaluation

In order to understand the usability of this robot, we have to evaluate its reachable workspace (i.e. all of the points in space its end-effector can reach from its fixed base). However, since this robot's intended use is for transthoracic procedures, we are only interested in evaluating its reachability across the surface of the human body – in this case, our human body model. Additionally, because the orientation of the needle end-effector is very important for the applications of this robot, we not only evaluate whether the poisiton of a point can be reached, but if it can be reached for a specified needle angle. Thus we sample points across the human body model and evaluate how "reachable" that point is by how many different collision-free configurations the robot can achieve that place its end-effector on the target point at a specified orientation.

To evaluate the robot reachable, collision-free work-space within the CT bore, three sets of over 7500 target needle end-effector poses across the full surface of the human body were uniformly sampled and evaluated for feasible joint configurations (more detail on finding joint configurations in Chapter 3). For consistency, the target orientation of each of these samples was held constant for each separate set. These orientations were set at 160°, 180°, and 200° with respect to the z-axis of the CT bed, respectively. Figure 2.3 gives a heat map for each set depicting the number of unique achievable configurations for a given target pose. For each sample, up to 10 joint configurations were sampled with a maximum of 100 trials per sample. These maps give us insight into what areas of the body are reachable when approached from various needle orientations, allowing more flexibility in the biopsy approach as well as highlighting the flexibility of the robot. Additionally, we can see how CRANE can be useful across multiple interventional radiology procedures, as it can reach a large area of the body given its initial position and configuration.

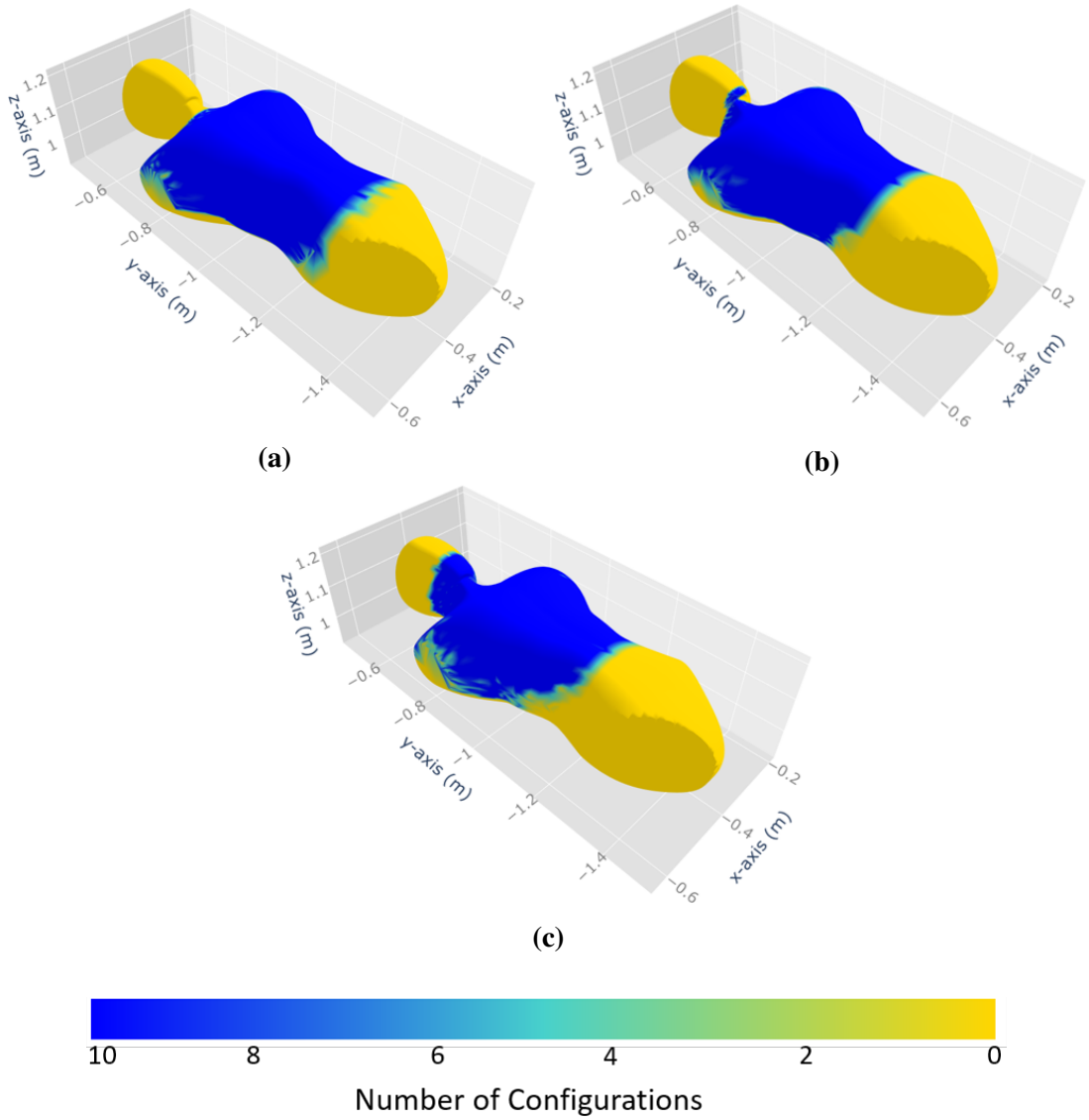

Figure 2.3. The reachable workspace for target poses with a) 160°, b) 180°, and c) 200° α angles.

Chapter 3

Obtaining Inverse Kinematics Solutions

The CRANE robot is a rigid multibody system consisting of a set of rigid links, joined together by both revolute (rotational) and prismatic (translational) joints. Therefore, we can control its movement via inverse kinematics (IK). For our scenario, it is presumed that a specified point at the end of the biopsy needle link, called the end effector, is assigned a target position and orientation. To solve this IK problem, we have to find settings for the joint angles such that the resulting configuration of the multibody places the end effector at its target position.

There are several methods for solving IK problems originating from robotics applications. These include Jacobian transpose methods [39],[40], pseudoinverse methods [41], the Levenberg-Marquardt damped least squares methods [42],[43], cyclic coordinate descent methods [44], quasi-Newton and conjugate gradient methods [44],[45], and neural net and artificial intelligence methods [46],[47]. For this paper, we utilize the first-order damped least squares (DLS) method due to its numerical stability.

3.1 Preliminaries

The complete configuration of the rigid multibody system is specified by $[q_1, ..., q_n]^T \in Q$, where Q is the configuration space (C-space), which describe the joints' configurations. Each q_j value represents either a joint angle or joint position for revolute and prismatic joints, respectively. For our model, we use only the first 7 joints of the robot, as the final insertion joint is used for

needle insertion once reaching the target pose. It is therefore excluded as we do not wish to change its joint position.

The distal tip of the biopsy needle is identified as the end-effector, with a pose that is a function of the joint angles and is denoted by $s \in Y$, where Y is our task space. In CoppeliaSim, the Euler angles describing the orientation of this end-effector and the entire rigid body are α, β and γ. They describe a rotation composed of three elemental rotations:

$$Q = R_x(\alpha) \cdot R_y(\beta) \cdot R_z(\gamma) \tag{3.1}$$

where R_x, R_y and R_z represent elemental rotations about the x, y and z axes respectively in the absolute reference frame. We write s as the column vector $\mathbf{s} = [x, y, z, \alpha, \beta]^T$, where the γ angle is not considered as the needle is symmetric around its γ axis (the z-axis of the end-effector frame is in line with the length of the needle). Finally, we denote our target pose for insertion as $\mathbf{t} = [x, y, z, \alpha, \beta]^T$. We let $\mathbf{e} = \mathbf{t} - \mathbf{s}$, the desired change in position of the end-effector.

The IK problem is to find values for the q_j's such that

$$\mathbf{t}_i = \mathbf{s}_i(\mathbf{q}), \qquad \text{for all i} \tag{3.2}$$

As there is no closed-form solution for this equation in our robot system, we use iterative methods to approximate a good solution. To do this, the functions s_i are linearly approximated using the Jacobian matrix, J. The Jacobian matrix is a function of the $\mathbf{q}$ values and is defined by

$$J(\mathbf{q}) = (\frac{\partial \mathbf{s}_i}{\partial q_j})_{i,j} \tag{3.3}$$

The equation for forward dynamics that defines the velocity of the end effector can be written as

$$\dot{\mathbf{s}} = J(\mathbf{q})\dot{\mathbf{q}} \tag{3.4}$$

Thus, the change in end-effector pose caused by a change in joint positions/angles can be

estimated as

$$\Delta \mathbf{s} \approx J \Delta \mathbf{q} \tag{3.5}$$

At each iteration, we update the joint angles $\mathbf{q}$ by $\Delta \mathbf{q}$: $\mathbf{q} := \mathbf{q} + \Delta \mathbf{q}$.

The joint angles are updated iteratively until a value of $\mathbf{s}$ is obtained that is sufficiently close to a solution. We therefore want to choose a $\Delta \mathbf{q}$ value such that $\Delta \mathbf{s}$ is approximately equal to $\mathbf{e}$. One approach to this problem is to solve the equation

$$\mathbf{e} = J \Delta \mathbf{q} \tag{3.6}$$

for $\Delta \mathbf{q}$. However, for this robotic platform, this equation cannot be solved uniquely as the Jacobian is not square.

3.2 Damped Least Squares (DLS) Method

It would seem natural to directly compute the inverse or Moore-Penrose pseudoinverse of J in equation 3.6, but this often leads to poor performance of the system due to instability near singularities. The DLS method (also known as the Levenberg-Marquardt method [42]) avoids this problem and gives a numerically stable method of selecting $\Delta \mathbf{q}$. Rather than find the minimum vector $\Delta \mathbf{q}$ that provides a best solution to equation 3.6, we find the value of $\Delta \mathbf{q}$ that minimizes the quantity

$$||J \Delta \mathbf{q} - \mathbf{e}||^2 + \lambda^2 ||\Delta \mathbf{q}||^2 \tag{3.7}$$

where $\lambda = \{\lambda \in \mathbb{R} | \lambda > 0\}$ is a damping constant. This is equivalent to minimizing the quantity

$$\left\| \begin{pmatrix} J \\ \lambda I \end{pmatrix} \Delta \mathbf{q} - \begin{pmatrix} \mathbf{e} \\ 0 \end{pmatrix} \right\| \tag{3.8}$$

And the subsequent normal equation becomes

$$\begin{pmatrix} J \\ \lambda I \end{pmatrix}^T \begin{pmatrix} J \\ \lambda I \end{pmatrix} \Delta\mathbf{q} = \begin{pmatrix} J \\ \lambda I \end{pmatrix}^T \begin{pmatrix} \mathbf{e} \\ 0 \end{pmatrix} \Rightarrow (J^T J + \lambda^2 I)\Delta\mathbf{q} = J^T\mathbf{e} \tag{3.9}$$

It can be shown that $(J^T J + \lambda^2 I)$ is non-singular, and thus the damped least squares solution becomes

$$\Delta\mathbf{q} = (J^T J + \lambda^2 I)^{-1} J^T \mathbf{e} \tag{3.10}$$

Because $J^T J \in \mathbb{R}^{m\times m}$, where m is the number of degrees of freedom (i.e. length of $\Delta\mathbf{q}$), we can show that $(J^T J + \lambda^2 I)^{-1} J^T = J^T (JJ^T + \lambda^2 I)^{-1}$ and therefore

$$\Delta\mathbf{q} = J^T (JJ^T + \lambda^2 I)^{-1} \mathbf{e} \tag{3.11}$$

The advantage of equation 3.11 is that it can be computed without needing to carry out the matrix inversion. Instead, row operations can solve for some vector $\mathbf{v}$ such that $(JJ^T + \lambda^2 I)\mathbf{v} = \mathbf{e}$. Since $\mathbf{v} = (JJ^T + \lambda^2 I)^{-1}\mathbf{e}$, the solution to equation 3.11 then becomes $\Delta\mathbf{q} = J^T\mathbf{v}$.

The damping constant used is dependent on the multibody itself and the target poses, and must be chosen such that equation 3.11 is numerically stable. It should large enough such that solutions for $\Delta\mathbf{q}$ are well-behaved near singularities, but not so large that the convergence rate is too slow. For this system, we choose $\lambda = 0.01$.

3.3 Task Augmentation

A manipulator is considered kinematically redundant if the number of DoF's is higher than the number of task space coordinates. For our needle placement scenario, the 7-DoF design (excluding the 1 DoF corresponding to needle advancement access) and five end-effector pose constraints allows for two redundant DoF. This space of redundant solutions can be exploited

to obtain a more versatile manipulator while having no affect on the overall motion of the end-effector. For our case, redundancy can be used to meet constraints on joint range availability and obtain trajectories in the joint space which are collision-free in the presence of obstacles along the motion.

In CoppeliaSim, this is done using the augmented or extended Jacobian matrix [48], where the kinematics of the CRANE arm are appropriately augmented to include the previously mentioned constraints, resulting in an efficient, fast, closed-loop algorithm which only makes use of the direct kinematics of the manipulator. The full method is given in Algorithm 1 and described in the following subsections.

For the sake of clarity, the two cases of obstacle avoidance and limited joint range are treated separately in the following subsections, but can be simultaneously considered when extending the task space vector and solving the inverse kinematic problem.

3.3.1 Obstacle Avoidance

One of the ways we utilize this kinematically redundant robotic system is the using the redundant DOF's to avoid contact with obstacles. Even if the arm is tracking a desired collision-free end-effector trajectory in the task space, one or more of its kinematic links may be too close to an obstacle in the workspace. As a result, one or more constraints must be introduced to avoid a collision with the obstacle.

It can be assumed that a link has avoided an obstacle if its minimum distance from the obstacle is greater than a given threshold distance (more on the calculation of this minimum distance in Chapter 5). If at each iteration all links satisfy this condition, the solution algorithm (equation 3.11) will select one of the infinite possible configurations, depending on the initial joint configuration. However, if the distance between one of the links and an obstacle becomes less than the threshold, the solution is modified.

We denote the threshold distance as $\hat{d}_o$. Once the minimum distance between a link and the closest obstacle is calculated, we denote the position vector of the point of interest

on the obstacle as $\mathbf{c}$ and the position vector of the point of interest on the link as $\mathbf{p}_o$. Both of these vectors are defined with respect to the world frame. It should be noted that the position of the minimum distance point moves as the robot arm moves about the obstacle and $\mathbf{p}_o$ must be recomputed along the trajectory. If the distance $||\mathbf{d}_o|| = ||\mathbf{p}_o - \mathbf{c}||$ between the two points becomes less than $\hat{d}_o$, the joint velocities must be modified. From our original error definition of $\mathbf{e} = \mathbf{t} - \mathbf{s}$ between desired and actual end-effector pose, an analogous definition of the obstacle avoidance error is defined in [49] as

$$e_o = 0.5(\hat{d}_o^2 - \mathbf{d}_o^T \mathbf{d}_o) \tag{3.12}$$

where $\mathbf{d}_o$ is the minimum distance between the link and the obstacle . Differentiating (3.12) with respect to time results in

$$\dot{e_o} = \hat{d}_o \dot{\hat{d}}_o - \mathbf{d}_o^T \dot{\mathbf{c}} - \mathbf{j}_{do}^T \dot{\mathbf{q}} \tag{3.13}$$

Assuming that all obstacles remain static and the threshold remains constant (as is the case in our environment), we get

$$\dot{e_o} = -\mathbf{j}_{do}^T \dot{\mathbf{q}} \tag{3.14}$$

where

$$\mathbf{j}_{do}^T = \mathbf{d}_o^T J_{po} \tag{3.15}$$

and J_{p_o} is the Jacobian matrix $\frac{\partial \mathbf{p}_o}{\partial \mathbf{q}}$ of the obstacle avoidance point $\mathbf{p}_o$. This vector, $\mathbf{j}_{do}^T$, represents the additional obstacle avoidance constraint row added to the end of the original Jacobian matrix to form the augmented Jacobian matrix. Once the minimum distance surpasses the threshold, this constraint can be released.

3.3.2 Limited Joint Range

Similarly, we can activate a mechanical constraint on a joint variable. We assume that each joint position or angle, q_j, is kinematically constrained between two constant extremal values: $q_{j,min} \leq q_j \leq q_{j,max}$. These extrema are known as joint limits of the joint q_j.

If the joint position or angle approaches either of these limits while the IK solver is executing, the solution is modified. Like what was done for obstacle avoidance, a threshold distance $\hat{d}_q$ can be defined as the minimum distance allowed between the current q_j and either of its two limits. We thus define the corresponding error as

$$e_q = \hat{d}_q - d_q \tag{3.16}$$

where $d_q = q_j - q_{j,min}$ or $d_q = q_{j,max} - q_j$ depending on which limit is involved. Differentiating (3.16) with respect to time and assuming $\hat{d}_q$ is constant gives

$$\dot{e}_q = -\mathbf{u}_j^T \dot{\mathbf{q}} \tag{3.17}$$

where

$$\mathbf{u}_j = \begin{pmatrix} 0 \\ \vdots \\ j = \pm 1 \\ \vdots \\ 0 \end{pmatrix} \tag{3.18}$$

The + and - signs apply to $q_{i,min}$ and $q_{i,max}$ respectively to move the joint position/angle in the appropriate direction. Once the minimum distance surpasses the threshold, this constraint can be released.

3.3.3 Overall Solution

Using the results of the two previous subsections, the overall solution algorithm to the IK problem for our constrained redundant manipulator can be established. Modifying our DLS control scheme in equation 3.11 results in

$$\Delta\mathbf{q} = J_a^T (J_a J_a^T + \lambda^2 I)^{-1} \mathbf{e_a} \tag{3.19}$$

where

$$J_a = \begin{bmatrix} J \\ J_{d_o} \\ U \end{bmatrix} \tag{3.20}$$

is the augmented Jacobian matrix which includes the original end-effector Jacobian J, J_{d_o} $(k \times 7)$ whose rows $\mathbf{j}_{d_o}^T$ are the k obstacle constraints defined in (3.15), and U $(r \times 7)$ whose rows are the r joint limit constraints defined in (3.18). We also have

$$\mathbf{e}_a = \begin{bmatrix} \mathbf{e} \\ \mathbf{e}_o \\ \mathbf{e}_q \end{bmatrix} \tag{3.21}$$

which is the augmented error vector in the task space including the original end-effector error vector $\mathbf{e}$, $\mathbf{e}_o$ $(k \times 1)$ with components defined in (3.12), and the error vector $\mathbf{e}_q$ $(r \times 1)$ with components defined in (3.16).

It should be noted that

$$m = k + r \leq 2 \tag{3.22}$$

so as to implement at most 2 constraints for our system's two redundant DoFs. If m is greater than 2, our system becomes overconstrained; however, the DLS control method can still compute a minimum-norm solution at each IK iteration. Based on the relative simplicity of our environment

and the initial configuration of the CRANE arm, we assume that the system will not often be overconstrained.

Algorithm 1. Task Augmentation

Input: $\mathbf{t} \in \mathbb{R}^5$

$\mathbf{q} \leftarrow \mathbf{q}_0$
for n in IK steps **do**
  $\mathbf{s} \leftarrow$ getPose(needleTip)
  $\mathbf{e} \leftarrow \mathbf{t} - \mathbf{s}$
  $J \leftarrow$ getJacobian(robot)
  for l in links **do**
    $\mathbf{d}_{l,o} \leftarrow$ minDistToObstacle(l)
    if $||\mathbf{d}_{l,o}|| < \hat{d}_o$ **then**
      $\mathbf{e}_{l,o}, \mathbf{j}^T_{l,d_o} \leftarrow$ obstacleAvoidance($\mathbf{d}_{l,o}$)
    end if
  end for
  for j in joints **do**
    $d_{j,q} \leftarrow$ minDistToJointLimits(q_j)
    if $d_{j,q} < \hat{d}_q$ **then**
      $e_{j,q}, \mathbf{u}^T_j \leftarrow$ limitedJointRange($d_{j,q}$)
    end if
  end for
  $J_a \leftarrow [J, J_{d_o}, U]^T$
  $\mathbf{e}_a \leftarrow [\mathbf{e}, \mathbf{e}_o, \mathbf{e}_q]^T$
  $\mathbf{q} \leftarrow \text{DLS}(J_a, \mathbf{e}_a)$
end for

3.4 Randomized Search to Obtain Multiple "Unique" IK Solutions

In order to move the robot from its initial position to its specified final insertion position, it may be necessary to move the end-effector over a relatively large distance. Because inverse kinematics is only stable for small $\Delta\mathbf{q}$ steps, the tip pose may be too far from the target pose to run IK successfully. Thus, we first use a randomized search in joint configuration space to place the end-effector within some specified threshold distance from the target position. The first seven joints are given a random joint position or angle, and forward kinematics is used to find the end-effector position in space. The Euclidean distance between the end-effector and target is

then computed and compared to a threshold. If the distance is within the threshold, IK is run to bring the tip onto the target. Else, the joints are given a new set of configurations and the process repeats. To limit this computation for unreachable targets, a maximum time of 10ms is assigned after which the search is aborted.

As we intend to rank multiple IK solutions for each needle target, we must find multiple "unique" joint configurations that achieve a given end-effector pose. For our particular problem, we define "unique" solutions as those that satisfy some distance threshold in C-space when compared to one another. We do not limit unique solutions to those that lie on separate configuration manifolds, as determining these self-motion groupings is a difficult and open research area and outside the scope of this thesis. For our purposes, it is less important that we determine the exact uniqueness of a solution than that we are able to generate multiple solutions with reasonably different behaviors. Once these configurations are collected, we implement the ranking metrics.

Chapter 4

Cone Maneuverability

For our transthoracic biopsy application, one of the criteria for a valid final joint configuration is manipulability around the target pose. While our goal is to place the robot in a final configuration that requires only linear translation of the needle to extract a tissue sample, we recognize that kinematic model inconsistencies with the real robot and tissue deformations may result in errors between the end-effector and specified target pose, or between the specified pose and the actual pose needed to reach the nodule.

To this end, for each joint configuration we densely sample nearby configurations that maneuver the biopsy needle around a local cone surface. We fix the end-effector position but adjust the rotation about the x axis of the needle by $\Delta\alpha_{needle}$. We assume that any adjustments that are made to the needle once it has entered the patient will be small (a few millimeters to a centimeter), and thus limit $\Delta\alpha$ to small values such as $5-10^{\circ}$. We then make 1° incremental adjustments to the rotation about the z axis in the absolute frame, $\Delta\gamma_w$, such that the trajectory of the length of the needle moves 360° in a counter-clockwise direction and forms the surface of a cone (see Figure 4.1). At each step, we use IK to find a new joint configuration and move the robot arm accordingly. This process terminates either when the entire cone surface has been traversed or when any of the joints have exceeded their limits. Finally, during post-processing, collision-checking is implemented at each step of the cone trajectory. This entire process is then repeated in the clockwise direction. Refer to Algorithm 2 for the step-by-step implementation.

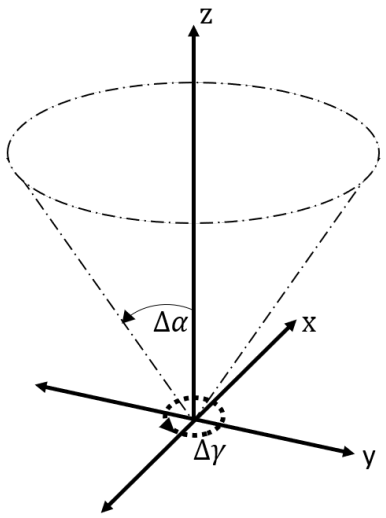

Figure 4.1. Depiction of conical movement of biopsy needle for maneuverability metric.

Figure 4.2 gives a simulated depiction of both a complete and incomplete cone trajectory. We see that for the incomplete trajectory, the joint configuration is initially so close to joint limits or singularities, that moving 10° along its x-axis is impossible.

The sampled joint configurations for a given target pose are denoted by $[\mathbf{q}_1, ..., \mathbf{q}_M]^T$ where each $\mathbf{q}_i$ represents the vector of joint positions/angles for the ith configuration. Each joint configuration is given a discrete score, $h_{cone}(\mathbf{q}_i)$, corresponding to the number of trajectory steps taken in each direction that were not in collision.

$$h_{cone}(\mathbf{q}_i) = \sum_{\psi=1}^{360} \mathbb{1}\{\mathbf{q} \in Q_{free}\} + \sum_{\psi=-1}^{-360} \mathbb{1}\{\mathbf{q} \in Q_{free}\} \tag{4.1}$$

Configurations with higher scores are deemed more maneuverable within a local cone volume around the target pose, giving radiologists more room to make slight adjustments to the needle when extracting a tissue sample, as well as giving them more confidence that the setup configuration will result in a successful procedure.

Algorithm 2. Cone Maneuverability

Input: $\Delta\alpha$,$\Delta\gamma_w, q_0$

$h_{cone} \leftarrow 0$
$[\alpha, \beta, \gamma] \leftarrow$ getOrientation(needleTip)
$\alpha \leftarrow \alpha + \Delta\alpha$
for i in $2\pi/\Delta\gamma_w$ **do**
    $T \leftarrow$ rotateAboutWorldZAxis($\Delta\gamma_w$)
    $\mathbf{t} \leftarrow$ setTargetTransformationMat($\mathbf{t}$,T)
    $\mathbf{q} \leftarrow$ IK($\mathbf{t}$)
    if q then
        setRobotJointPositions($\mathbf{q}$)
        if $\mathbf{q}_{min} \leq \mathbf{q} \leq \mathbf{q}_{max}$ and $\mathbf{q} \in Q_{free}$ **then**
            $h_{cone} \leftarrow h_{cone} + 1$
        end if
    else
        Break
    end if
end for
$\mathbf{q} \leftarrow \mathbf{q}_0$
for i in $2\pi/\Delta\gamma_w$ **do**
    $T \leftarrow$ rotateAboutWorldZAxis($-\Delta\gamma_w$)
    $\mathbf{t} \leftarrow$ setTargetTransformationMat($\mathbf{t}$,T)
    $\mathbf{q} \leftarrow$ IK($\mathbf{t}$)
    if q then
        setRobotJointPositions($\mathbf{q}$)
        if $\mathbf{q}_{min} \leq \mathbf{q} \leq \mathbf{q}_{max}$ and $\mathbf{q} \in Q_{free}$ **then**
            $h_{cone} \leftarrow h_{cone} + 1$
        end if
    else
        Break
    end if
end for

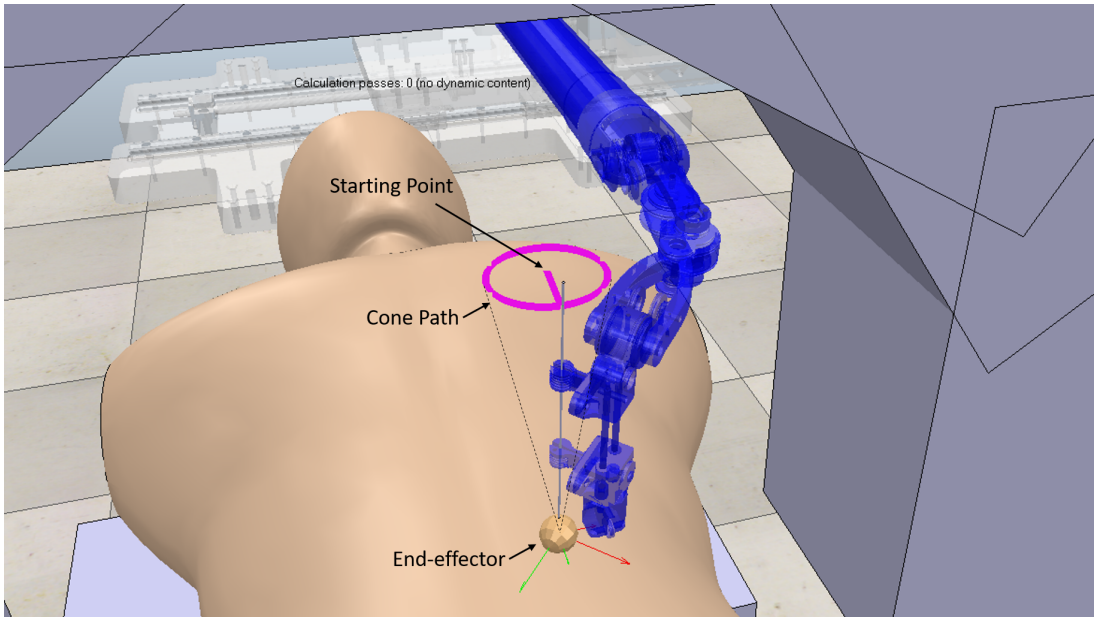

(a)

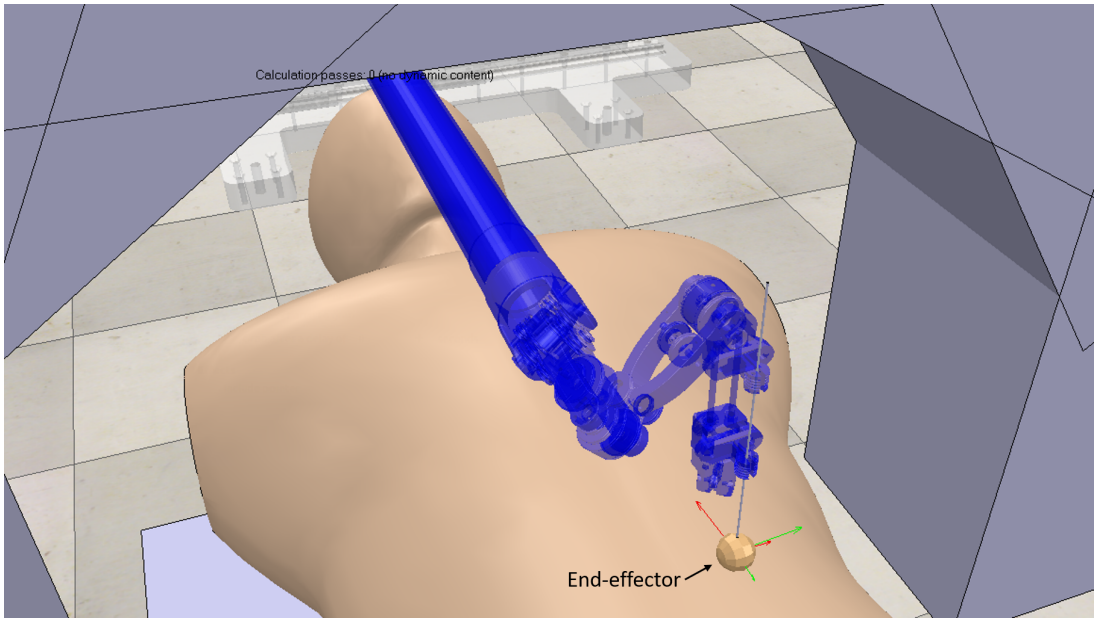

(b)

Figure 4.2. Example of a a) complete and b) incomplete cone movement of the CRANE needle. The brown orb at the end of the arm represents the needle tip end-effector. The pink curve in a) represents the movement of the needle end around the cone surface, with a starting position in the center of the circle.

Chapter 5

Ranking IK Solutions and Planning

5.1 Additional Metrics

In addition to scoring joint configurations based on their maneuverability within a local cone volume, we consider several other ranking metrics when evaluating possible joint configurations for a desired needle tip pose. These include: distance from joint limits, distance to collision, and distance to singularities.

5.1.1 Joint Limit Avoidance

Each of the 8 joints in this robotic system have degrees of freedom which are subject to joint limits. While obtaining valid joint configurations for a needle target, our IK solver uses the nullspace of the system for joint limitation constraints. However, this constraint only serves to keep the joint positions and angles within their limits, and does not try to maximize the distance from the joint limits.

When comparing across multiple valid joint configurations for a given target, we want to maximize the joint's "distance" from both of its limits. Again, the sampled joint configurations for a given target pose are denoted by $[\mathbf{q}_1, ..., \mathbf{q}_N]^T$ where each $\mathbf{q}_i$ represents the vector of joint positions/angles for the ith configuration. Given $q_{i,j} \in [q_{i,j,min}, q_{i,j,max}]$ where $q_{i,j}$ value represents the jth joint angle/position in the ith configuration, we find the minimum distance (in meters) from the joints limits and use a 2-norm to find the total distance from joint limits of each

sampled joint configuration:

$$h_{joint}(\mathbf{q}_i) = \sqrt{\sum_{j=1}^{7} (\min[q_{i,j} - q_{i,j,min}, q_{i,j,max} - q_{i,j}])^2} \tag{5.1}$$

This total distance measurement is used as a joint limit score for each configuration.

5.1.2 Distance to Collision

As the CRANE robot operates within the limited free space inside the CT bore and around the patient, it is imperative that all sampled joint configurations are out of collision. CoppeliaSim uses its own collision checking and minimum distance calculation routines. The method is based on a hierarchy of object-oriented bounding boxes that wrap triangles composing mesh shapes in the scene [50]. Using this method, detection and distance calculations are triangle-triangle exact. Using nullspace control during configuration sampling, our IK solver finds valid configurations that are out of collision. However, similar to the joint limit constraint, this collision-free constraint only serves to keep the robot out of collision, and does not try to maximize the distance from collision.

Thus, for each configuration, we find the minimum distance to collision for each of the robot arm links that enter the CT bore. These include the four links of the 4-DoF intra-bore stage, as well as the final link in the 4-DoF exo-bore stage that partially enters the bore. The collision obstacles considered are the CT bore, the CT bed, and the patient themselves. For our obstacle avoidance metric, we want to maximize the minimum distance to Cartesian obstacles (also known as clearance) using the Euclidean 2-norm.

$$h_{coll}(\mathbf{q}_i) = \min_{\substack{a \in \text{robot links} \\ b \in \text{obstacles}}} ||a(\mathbf{q_i}) - b||_2 \tag{5.2}$$

This total distance measurement in meters is then used as a distance to collision score for each configuration.

5.1.3 Distance to Singularities

The final metric we evaluate over is a configuration's distance from singularities. When controlling a manipulator in Cartesian space, we sometimes run into singularities or degeneracies when mapping from Cartesian space to joint configuration space. Some types of singularities include:

1. "Losing a DoF": At a singularity, the mobility of a manipulator is reduced and usually, arbitrary motion of the manipulator in a Cartesian direction is lost.

2. Boundary Singularities: A common type of singularity, usually caused by a full extension of a joint, where the manipulator is asked to move beyond where it can be positioned. Typically, this is trying to reach out of the workspace at the farthest extent of the workspace.

3. Internal Singularities: These singularities are generally caused by an alignment of the robot's axes in space. For example, if two axes become aligned in space, the rotation of one can be canceled by counter-rotation of the other, leaving the actual joint location indeterminate. Additionally, certain kinematic alignments specific to the manipulator can cause these.

At a joint space singularity, infinite inverse kinematic solutions may exist, and small Cartesian motions may require infinite joint velocities.

It is important then to consider these singularities when evaluating potential joint configurations for a target needle pose. Even if the configuration itself is not a singularity, it may be near a singularity that will cause issues when slight adjustments to the arm are made during the biopsy procedure. We therefore evaluate the distance in C-space to singularities using the Jacobian matrix of the arm. Yoshikawa's manipulability index introduced a quality measure for redundant manipulators which describes their distance to singular configurations [51]. The measure is based on analyzing the manipulability ellipsoid that is spanned by the singular vectors of the Jacobian. The equation for this singularity distance metric is

$$h_{sing}(\mathbf{q}_i) = \sqrt{\det[J(\mathbf{q}_i)J^T(\mathbf{q}_i)]} = s_1 s_2 ... s_N \tag{5.3}$$

where each s_i represents the singular values of the Jacobian matrix. Thus, this metric is proportional to the volume of the manipulability ellipsoid of the arm when in a specific configuration.

5.2 Weighting Scores

Given all of our defined ranking metrics, we can now linearly combine the scores using appropriate weightings.

$$h_{weighted}(\mathbf{q}_i) = \rho_{cone} h_{cone}(\mathbf{q_i}) + \rho_{joint} h_{joint}(\mathbf{q_i}) + \rho_{coll} h_{coll}(\mathbf{q_i}) + \rho_{sing} h_{sing}(\mathbf{q_i}) \tag{5.4}$$

where each ρ is the corresponding weighting of that score. We place a constraint on this linear combination, requiring that the sum of all ρ values is equal to 1.

Additionally, we scale each unweighted score in order to rectify the differences in order of magnitude across the various metrics and make our final score unitless. For simplicity, we choose average normalization. Thus each score is divided by the average score obtained across all targets for that particular metric.

5.3 Path Planning

Finally, given the weighted scores for each sampled configuration for a specified end-effector pose, we choose the configuration with the highest score and use a planner to find a collision-free path from our initial robot configuration to this configuration in C-space. CoppeliaSim offers path/motion planning functionality via a plugin wrapping the OMPL (Open Motion Planning Library). Due to its convergence towards an optimal solution, we utilize the RRT* algorithm for path planning. An example of a generated path found in simulation between

the initial robot pose and the highest ranked configuration for the specified target pose is depicted in Figure 5.1.

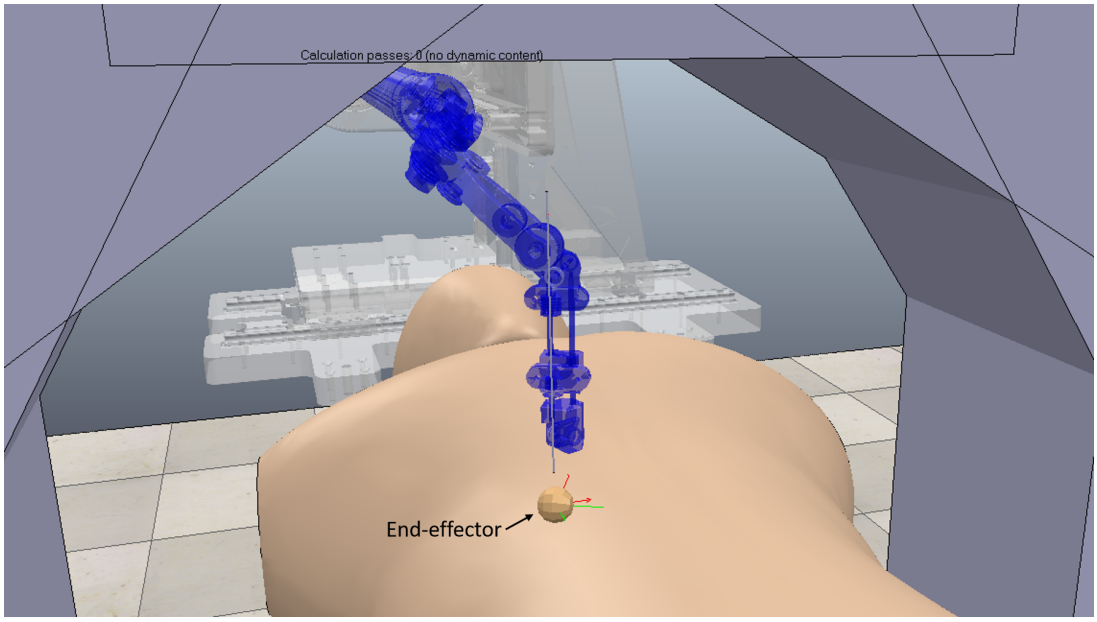

(a)

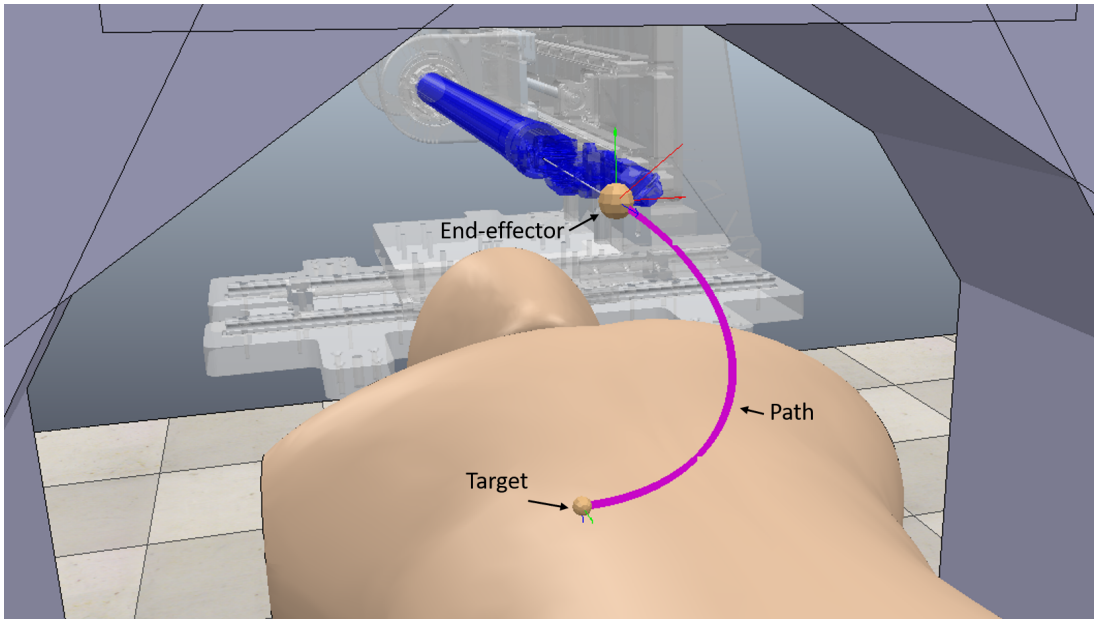

(b)

Figure 5.1. Example of a) an IK setup configuration and b) corresponding path generated using RRT* algorithm. The brown orb at the end of the arm represents the needle tip end-effector. The pink curve represents the end-effector path to the desired joint configuration and target needle pose.

Chapter 6

Experimental Results

6.1 Evaluation of Chosen Metrics

Figure 6.1 depicts the total scores, average scores, as well as the spread of scores across each metric for approximately 1000 targets sampled on the anterior surface of the body model with target vectors perpendicular to the CT bed (i.e. the needle is pointing directly down into the patient). Note that this data presented only includes targets which generated at least one successful IK configuration and a maximum of 50 configurations.

For our cone maneuverability metric data below, we chose a $\Delta\alpha$ value of 10° It is interesting to note that for the vast majority of targets, "fully maneuverable" configurations within this cone are possible, as seen by the large number of configurations that achieve the maximum cone maneuverability score (Figure 6.1a). However, in the same subfigure we can see that there are also a significant number of configurations that have little to no range of movement within this volume. Similarly, when looking at the score spread across each target (Figure 6.1b), we can see that a vast majority of targets have both very maneuverable configurations and configurations that essentially lock the arm in place. This further motivates our cone metric, as it is evident that even if an arm setup configuration is valid and reaches the target, it can be vastly superior or inferior to others.

When looking at the distance to joint limits and distance to collisions scores, we see a similar phenomenon as with the cone maneuverability metric, but with greater variability in

scores for each metric. The average scores per target for each of these metrics (Figure 6.1f and Figure 6.1i) display approximately Gaussian patterns, showing that on average the distance to joint limits and distance to collisions of the setup configurations for each target are approximately equidistant from the minimum and maximum allowable values.

Turning our attention to the distance to singularities, we see that in Figure 6.1j, many of the configurations generated are very near singularities in the C-space. Looking closely at the spread of scores in Figure 6.1k, it is evident that the difference in singularity distance between configurations reaching the same target pose can be great. As mentioned in Chapter 5, these singularities can arise in various forms, but as the configuration space of this robot has yet to be thoroughly explored and studied, these results may motivate further work on the subject. However, even without full knowledge of CRANE's C-space, this singularity metric allows us to find at least one configuration per target that lies reasonably within the bounds of a particular manifold.

6.2 Weighting Scores Across Needle Orientations

As we are interested in comparing the feasibility of various configurations to a particular target, we are also interested in comparing the feasibility of targets themselves. For one particular tissue nodule of interest, it may be possible to approach from several different positions and corresponding orientations. Because of how we define our ranking metrics and optimization over them, we can compare possible robot arm configurations across multiple targets in a straightforward manner. Figure 6.2 presents the average weighted scores received by configurations for each target position at various orientations and with various weighting combinations. We see particularly that as the weighting for cone maneuverability is increased, the number of targets with high average scores decreases. Additionally, as the α-orientation value is increased, the average scores tend to decrease as well. These results display the trade offs encountered when selecting a target approach vector and achieving high confidence in maneuverability of the robot

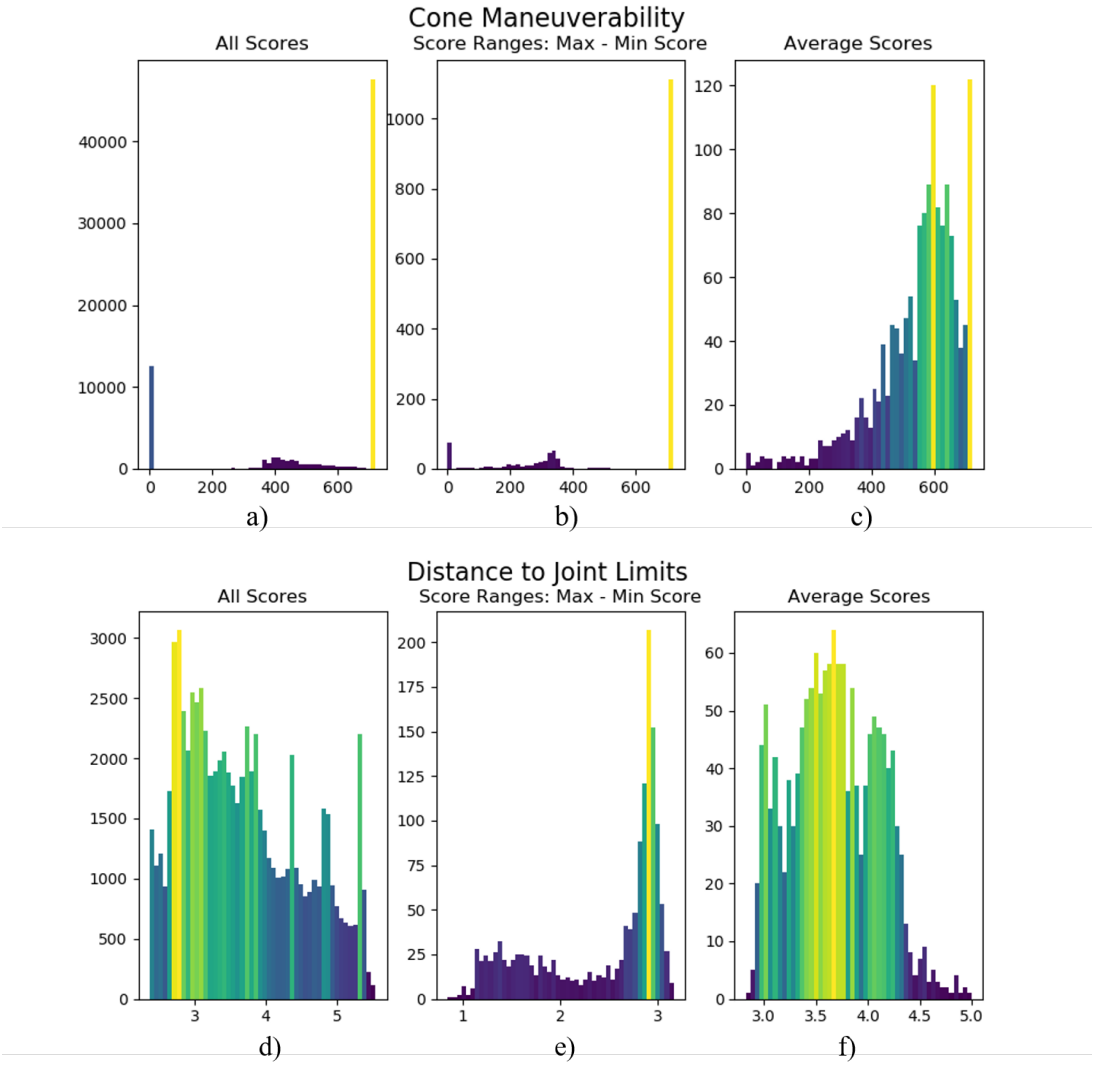

Figure 6.1. Scores for each configuration metric including: 1) all scores across all targets, 2) average scores across all targets, and 3) spread of scores across targets. Approximately 1000 targets are sampled on the anterior surface of the body model with target vectors perpendicular to the CT bed.

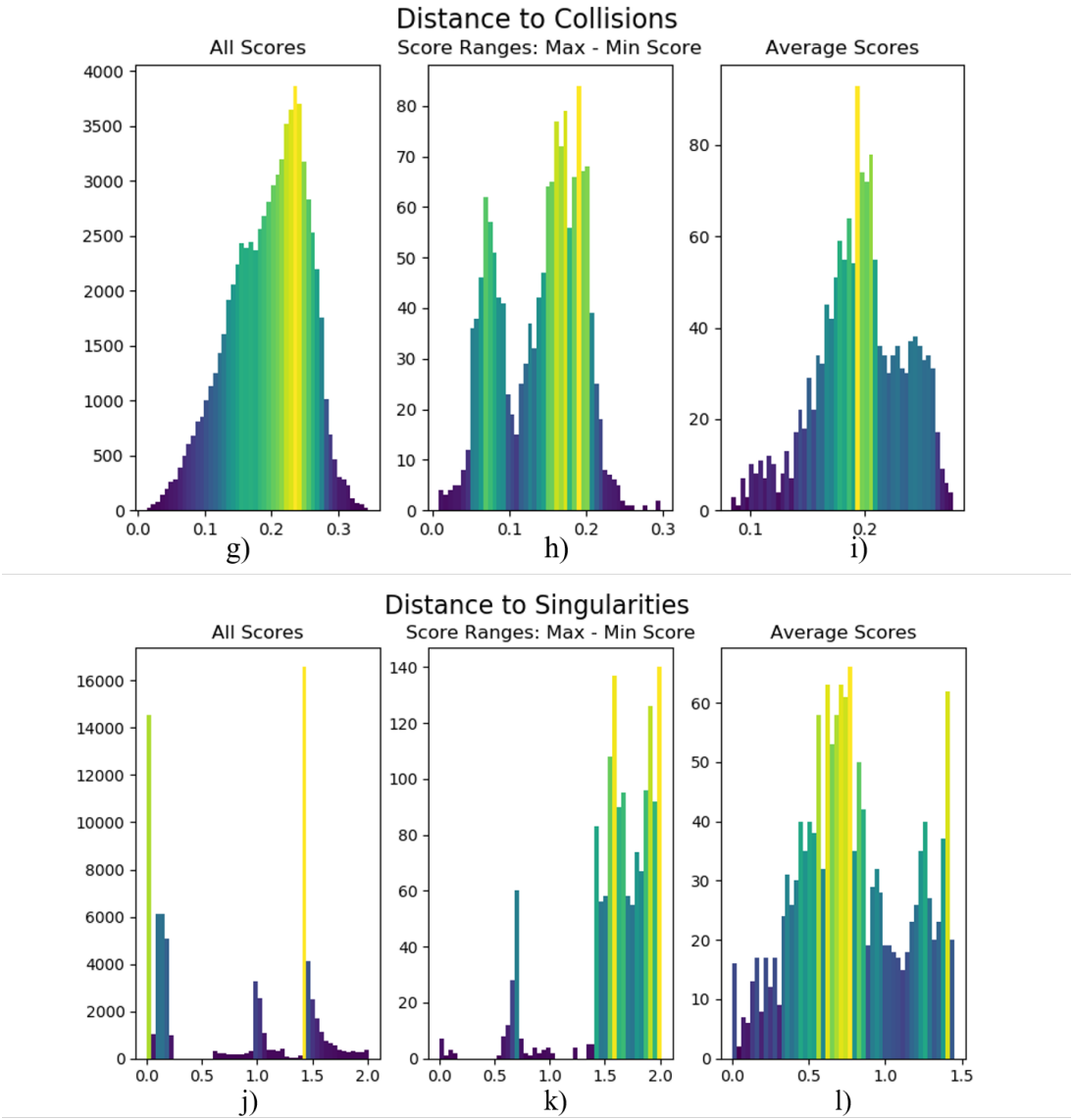

Figure 6.1. Scores for each configuration metric including: a) all scores across all targets, b) average scores across all targets, and c) spread of scores across targets. Approximately 1000 targets are sampled on the anterior surface of the body model with target vectors perpendicular to the CT bed, Continued.

once it has reached its setup configuration.

To visualize the effects of these weighting scores and confirm our results, Figure 6.3 presents examples of the highest ranked configurations for our different weighting combinations. We see that increasing the cone maneuverability weighting somewhat straightens the last few links of the robot arm to make it them more easily maneuverable in the local cone volume around the end-effector (Figure 6.3b). This is at the expense of the distance to collision, however, as we see that the $5th$ link of the arm extending into the CT bore is very close to the top of the CT bore. As expected, when increasing the relative weighting of the distance to collision metric (Figure 6.3c), the CRANE arm moves away from the top of the CT bore.

Figure 6.4 depicts the average weighted scores for a single target on the anterior surface of the chest at various needle -orientations. The weightings used for this experiment are $\rho_{cone} = 0.4$ and $\rho_{joint} = \rho_{coll} = \rho_{sing} = 0.2$. We can see that the scores trend downward as the needle is moved further and further from its original α-orientation with some intermittent fluctuation. These fluctuations can be attributed to several possible phenomena, including randomness in the configuration seeding or reaching the edge of a configuration manifold before moving to another one in the subsequent orientation step. Based on this plot, we see that while many approach vectors for a single target are possible, as the robot arm is forced to rotate the needle further from its starting orientation, other attributes such as range of motion and ease of maneuverability must be somewhat sacrificed.

6.3 End-to-End Control Scheme

An important question to ask is how long this proposed end-to-end control scheme we have presented takes to execute. In real applications and procedures, we want our algorithm to generate IK solutions, evaluate and rank them, and plan to the optimal configuration within a reasonable amount of time, such that the benefits of this robotic approach to needle biopsies are not offset by its run-time. Table 6.1 depicts the average speed of various checks and calculations

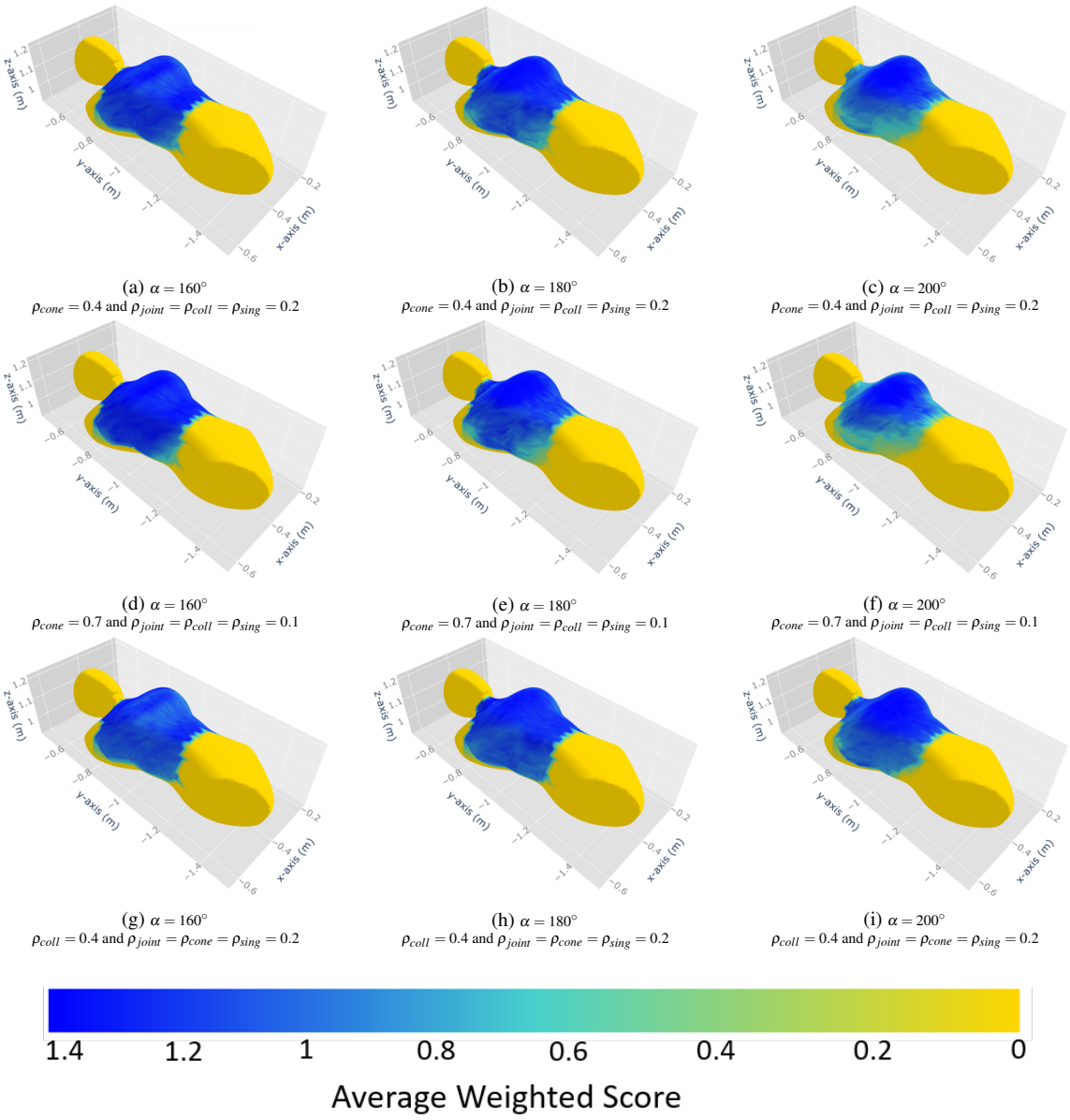

(a) $\alpha = 160°$
$\rho_{cone} = 0.4$ and $\rho_{joint} = \rho_{coll} = \rho_{sing} = 0.2$

(b) $\alpha = 180°$
$\rho_{cone} = 0.4$ and $\rho_{joint} = \rho_{coll} = \rho_{sing} = 0.2$

(c) $\alpha = 200°$
$\rho_{cone} = 0.4$ and $\rho_{joint} = \rho_{coll} = \rho_{sing} = 0.2$

(d) $\alpha = 160°$
$\rho_{cone} = 0.7$ and $\rho_{joint} = \rho_{coll} = \rho_{sing} = 0.1$

(e) $\alpha = 180°$
$\rho_{cone} = 0.7$ and $\rho_{joint} = \rho_{coll} = \rho_{sing} = 0.1$

(f) $\alpha = 200°$
$\rho_{cone} = 0.7$ and $\rho_{joint} = \rho_{coll} = \rho_{sing} = 0.1$

(g) $\alpha = 160°$
$\rho_{coll} = 0.4$ and $\rho_{joint} = \rho_{cone} = \rho_{sing} = 0.2$

(h) $\alpha = 180°$
$\rho_{coll} = 0.4$ and $\rho_{joint} = \rho_{cone} = \rho_{sing} = 0.2$

(i) $\alpha = 200°$
$\rho_{coll} = 0.4$ and $\rho_{joint} = \rho_{cone} = \rho_{sing} = 0.2$

Figure 6.2. Average weighted scores across targets on the human body model at various needle orientations and weighting combinations. Each row of the subfigure grid corresponds to a different weighting combination, while each column corresponds to a different needle orientation.

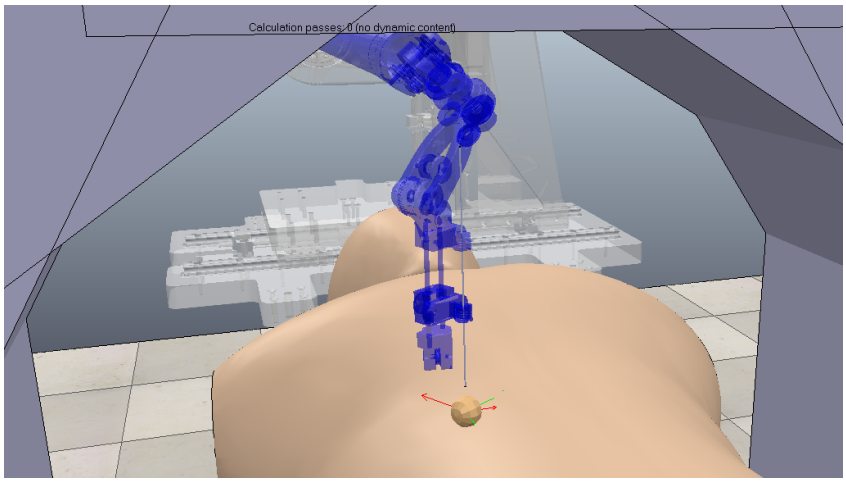

(a) $\rho_{cone} = 0.4$ and $\rho_{joint} = \rho_{coll} = \rho_{sing} = 0.2$

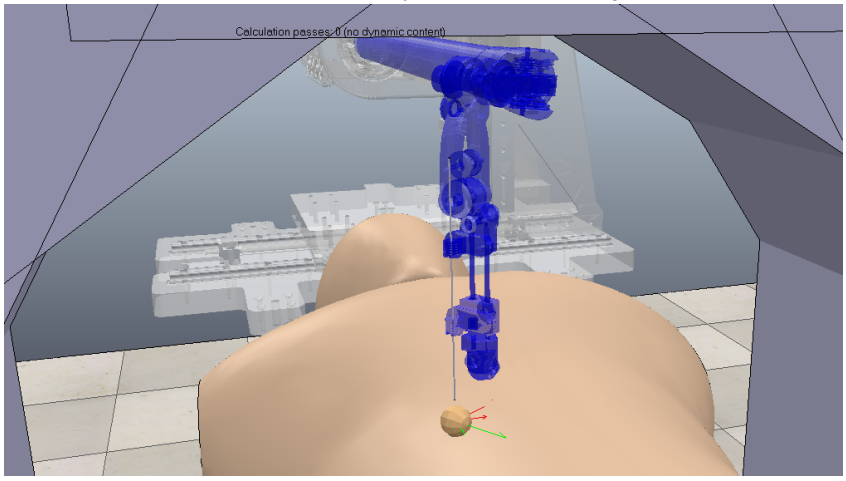

(b) $\rho_{cone} = 0.7$ and $\rho_{joint} = \rho_{coll} = \rho_{sing} = 0.1$

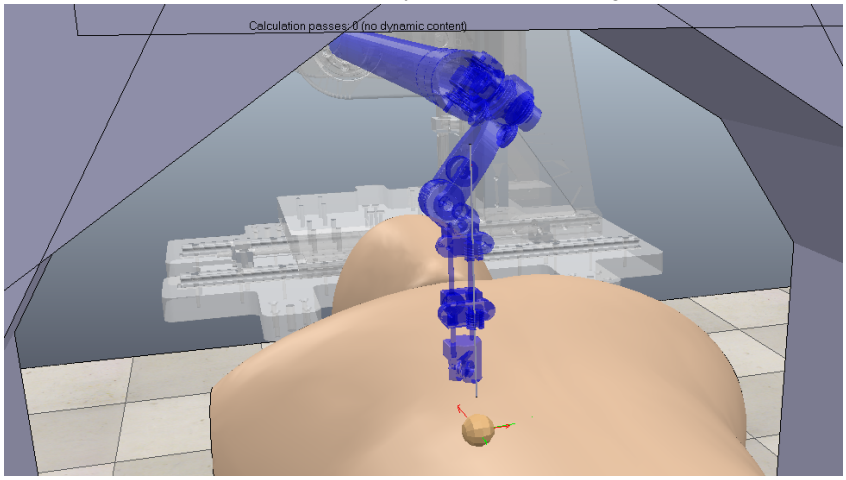

(c) $\rho_{coll} = 0.4$ and $\rho_{joint} = \rho_{cone} = \rho_{sing} = 0.2$

Figure 6.3. Highest ranked configuration for a given target with various metric weighting combinations.

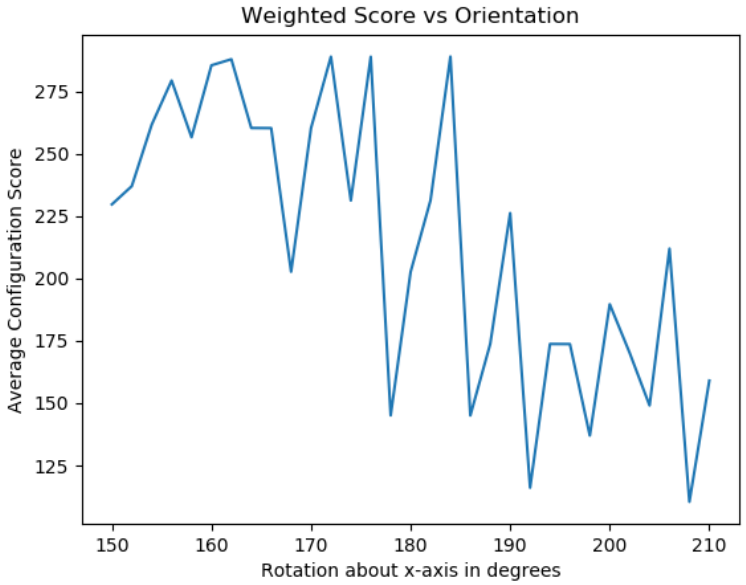

Figure 6.4. The average weighted configuration scores for a single target on the anterior surface of the chest at various needle α-orientations. 180° corresponds to the negative z-axis of the needle aligned perpendicular to the CT bed, representing a 90° rotation from the original needle z-axis orientation.

of interest within the algorithm, as well as the speed of execution for the entire algorithm given one target of interest.

Table 6.1. Speed of execution for calculations of interest and entirety of end-to-end control scheme. The full algorithm used for these calculations samples up to 10 valid configurations per target.

Calculation	Execution Time
Collision Checking	$4.2\mu s$
Distance to Collision	$2\mu s$
Joint Distance from Limits	$57\mu s$
Full Cone Movement (Per Configuration)	4.36s
Path Planning and Execution	24.14s
Full Algorithm	94.09s

We can see that in the span of one and a half minutes, we are able to take a specified needle pose, optimize a valid IK configuration to it, plan a collision-free path to it, and execute that plan. It should also be noted that if several targets poses are given as input, the speed of

execution will be less than the linear sum of the speed for those individual targets. This is because the path planning and execution will only execute once for the chosen configuration (and corresponding target pose).

Finally, we find that for 100 randomly chosen needle target poses across the ”reachable workspace” of our environment on the anterior surface of the human model, we are able to successfully generate collision-free paths to the highest-ranked configuration for every one.

Chapter 7

Conclusion

7.1 Discussion and Future Work

The goal of this thesis was to show a fully automated control scheme for the CRANE robotic platform that chooses a ”best” setup configuration by optimizing over several defined metrics and planning to that configuration. In addition to this, we have validated these metric choices by showing their ability to distinguish well among several candidate solutions.

It is important to note that while our choice of cone metric was well-informed, we acknowledge that it is somewhat arbitrary and that there are potentially other methods that could perform just as well if not better. However, our intention is to introduce the idea of evaluating a configuration based on its maneuverability within some local volume near the final end-effector pose and the chosen metric performed well in distinguishing among solutions. Other methods could include a conical spiral pattern, that moves the needle around cones of ever-increasing diameter. Similarly, our score normalization method is one of many possible choices and future work may experiment with these other methods.

A disadvantage of several of our current metrics are their non-differentiability. Our cone metric is a discrete function and our distance to collision metric is a max-min problem. This prevents us from taking the gradient of these metrics with respect to the joint values, q, and tuning our configurations to optimize these scores. We also note that our distance to joint limits metric is non-differentiable when $q_{i,j} - q_{i,j,min} = q_{i,j,max} - q_{i,j}$ for a given joint.

While the intention of this thesis is not to critically evaluate the mechanical design of this robot, our results give some interesting insight into its collision-free configuration space. Almost half of all configurations generated were at or very near singularities, which speaks both to the complexity of this 8-DoF robotic design, as well at the complexity of an imaging bore environment. A further extension to this work would be to evaluate configuration space, as well as the self-motions and homotopies of this redundant robotic manipulator. While we currently evaluate and score every randomly seeded configuration generated for a specific target pose, grouping configurations that lie on the same nullspace manifold allows us to simply produce one score for each grouping of configurations, thus reducing computation time and omitting potentially redundant solutions.

Additional future work will also include evaluating targets and corresponding configurations on other areas of the surface of the body. For a specific tissue sample or patient, it may be ideal to approach from the lateral or posterior surface of the body. As we are already able to compare across potential targets on the anterior surface, it would be a simple extension to compare across targets on multiple surface areas of the body.

Finally, another future goal of this work is to further automate the procedure by specifying potential target vectors without requiring an input from the radiologist. Given CT scan data, learning methods can be employed to generate one or several potential approach vectors to the nodule. This result can then be used as an input to the control scheme presented here. We still maintain the human-in-the-loop by allowing for validation steps at each stage of the process and maintaining manual insertion and adjustments of the needle once it has reached its setup configuration.

7.2 Summary

In this thesis, we demonstrated a ”smart” end-to-end automated control scheme for the CRANE robotic platform that optimizes a robotic configuration over several defined metrics

relevant to the successful completion of a transthoracic needle biopsy procedure. Given the significant challenges faced when performing precise needle biopsies within a CT bore, our chosen ranking metrics are able to successfully tease out the subtle differences between configurations and delineate between them effectively. This allows for a highly informed selection of setup needle targets and corresponding robot configurations, providing greater confidence that the procedure can be completed successfully without the need for simulation verification while also allowing for slight adjustments due to kinematic inaccuracies. In less than a few minutes, our control scheme can take several potential target approach vectors, find the optimal ranked configuration for each target and the optimal one among them, and execute a feasible, collision-free path to the chosen configuration.

Bibliography

[1] *American Cancer Society, Key Statistics for Lung Cancer*, 2019 (accessed April 8, 2020). [Online]. Available: https://www.cancer.org/cancer/non-small-cell-lung-cancer/about/key-statistics.html

[2] A. McLean, D. Barnes, and L. Troy, "Diagnosing lung cancer: the complexities of obtaining a tissue diagnosis in the era of minimally invasive and personalised medicine," *Journal of Clinical Medicine*, vol. 7(7):163, 2018.

[3] G. Shrieber and D. McCroy, "Performance characteristics of different modalities for diagnosis of suspected lung cancer: Summary of published evidence," *Chest*, vol. 123(1 Suppl):115S-128S.

[4] W. Baalini, M. Reinoso, A. Gorin, A. Sharafkaneh, and P. Manian, "Diagnostic yield of fiberoptic bronchoscopy in evaluating solitary pulmonary nodules," *Chest*, vol. 117:1049–1054.

[5] P. Rivera, A. Mehta, and M. Wahidi, "Establishing the diagnosis of lung cancer: Diagnosis and management of lung cancer: American college of chest physicians evidence-based clinical practice guidelines," *Chest*, vol. 143:e143S–e165S.

[6] P. Tian, Y. Wang, L. Li, Y. Zhou, W. Luo, and W. Li, "Ct-guided transthoracic core needle biopsy for small pulmonary lesions: Diagnostic performance and adequacy for molecular testing," *Journal of Thoracic Disease*, vol. 9, no. 2.

[7] W. Heerink, G. de Bock, G. de Jonge, H. Groen, R. Vliegenthart, and M. Oudkerk, "Complication rates of ct-guided transthoracic lung biopsy: meta-analysis," *European radiology*, vol. 27, no. 1.

[8] A. Manhire, M. Charig, C. Clelland, F. Gleeson, R. Miller, H. Moss, K. Pointon, C. Richardson, and E. Sawicka, "Guidelines for radiological guided lung biopsy," *Thorax*, vol. 58.

[9] E. Kazerooni, F. Lim, A. Mikhail, and F. Martinez, "Risk of pneumothorax in ct-guided transthoracic needle aspiration biopsy of the lung," *Radiology*, vol. 198.

[10] K. Yeow, L. See, K. Lui, M. Lin, T. Tsao, K. Ng, and H. Liu, "Risk factors for pneumothorax and bleeding after ct-guided percutaneous coaxial cutting needle biopsy of lung lesions," *J. Vasc. Interv. Radio*, vol. 12.

[11] J. Kettenbach and G. Kronreif, "Robotic systems for percutaneous needle-guided interventions," *Minimally Invasive Therapy Allied Technologies*, vol. 24, no. 1.

[12] S. B. Solomon, A. Patriciu, M. E. Bohlman, L. R. Kavoussi, and D. Stoianovici, "Robotically driven interventions: a method of using ct fluoroscopy without radiation exposure to the physician," *Radiology*, vol. 225, no. 1.

[13] Y. Moon, J. B. Seo, and J. Choi, "Development of new end-effector for proof-of-concept of fully robotic multichannel biopsy," *IEEE/ASME Transactions on Mechatronics*, vol. 20, no. 6.

[14] E. Ben-David, M. Shochat, I. Roth, I. Nissenbaum, J. Sosna, and S. N. Goldberg, "Evaluation of a ct-guided robotic system for precise percutaneous needle insertion," *Journal of Vascular and Interventional Radiology*.

[15] M. Anzidei, R. Argiro, A. Porfiri, F. Boni, M. Anile, F. Zaccagna, D. Vitolo, L. Saba, A. Napoli, A. Leonardi, F. Longo, F. Venuta, M. Bezzi, and C. Catalano, "Preliminary clinical experience with a dedicated interventional robotic system for ct-guided biopsies of lung lesions: a comparison with the conventional manual technique," *European radiology*, vol. 25, no. 5.

[16] A. Kuntz, P. J. Swaney, A. Mahoney, R. H. Feins, Y. Z. Lee, R. W. III, and R. Alterovitz, "Toward transoral peripheral lung access: Steering bronchoscope-deployed needles through porcine lung tissue," 2016, pp. 9–10.

[17] R. Monfaredi, K. Cleary, and K. Sharma, "Mri robots for needlebased interventions: Systems and technology," *Annals of Biomedical Engineering*, vol. 46.

[18] H. Dou, S. Jiang, Z. Yang, L. Sun, X. Ma, and B. Huo, "Design and validation of a ct-guided robotic system for lung cancer brachytherapy," *Medical physics*, vol. 44, no. 9.

[19] Y. Zhou, K. Thiruvalluvan, L. Krzeminski, W. H. Moore, Z. Xu, and Z. Liang, "An experimental system for robotic needle biopsy of lung nodules with respiratory motion," 2011.

[20] N. Hungr, I. Bricault, P. Cinquin, and C. Fouard, "Design and validation of a ct-and mri-guided robot for percutaneous needle procedures," *IEEE Transactions on Robotics*, vol. 32, no. 4.

[21] C. J. Walsh, N. Hanumara, A. Slocum, R. Gupta, and J.-A. Shepard, "Evaluation of a patient-mounted, remote needle guidance and insertion system for ct-guided, percutaneous lung biopsies," 2007, pp. 39–40.

[22] S. F. Atashzar, I. Khalaji, M. Shahbazi, A. Talasaz, R. V. Patel, and M. D. Naish, "Robot-assisted lung motion compensation during needle insertion," 2013, pp. 1682–1687.

[23] J. R. Rojas-Solano, L. Ugalde-Gamboa, and M. Machuzak, "Robotic bronchoscopy for diagnosis of suspected lung cancer: a feasibility study," *Journal of bronchology interventional pulmonology*, vol. 25, no. 3.

[24] Y. Han, H. J. Kim, K. A. Kong, S. J. Kim, S. H. Lee, Y. J. Ryu, J. H. Lee, Y. Kim, S. S. Shim, and J. H. Chang, "Diagnosis of small pulmonary lesions by transbronchial lung biopsy with radial endobronchial ultrasound and virtual bronchoscopic navigation versus ct-guided transthoracic needle biopsy: A systematic review and metaanalysis," *PloS one*, vol. 13, no. 1.

[25] K. B. Reed, A. Majewicz, V. Kallem, R. Alterovitz, K. Goldberg, N. J. Cowan, and A. M. Okamura, "Robot-assisted needle steering," *IEEE robotics automation magazine*, vol. 18, no. 4.

[26] *Intuitive Surgical, Inc.*, 2019 (accessed April 8, 2020). [Online]. Available: https://www.intuitive.com/en/products-and-services/ion

[27] P. J. Swaney, A. W. Mahoney, B. I. Hartley, A. A. Remirez, E. Lamers, R. H. Feins, R. Alterovitz, and R. J. W. III, "Toward transoral peripheral lung access: Combining continuum robots and steerable needles," *Journal of medical robotics research*, vol. 2, no. 1.

[28] J. G. Aerts, "Transthoracic needle biopsies: It's more than just hitting the bull's-eye," *Clinical Cancer Research*, vol. 22, no. 2.

[29] *Auris Health, Inc., Monarch Platform - Endoscopy Transformed*, 2019 (accessed April 8, 2020). [Online]. Available: https://www.aurishealth.com/monarch-platform

[30] J. S. W. Memoli, P. J. Nietert, and G. A. Silvestri, "Meta-analysis of guided bronchoscopy for the evaluation of the pulmonary nodule," *Chest*, vol. 142, no. 2.

[31] D. Fielding, F. Bashirzadeh, J. H. Son, M. Todman, H. Tan, A. Chin, K. Steinke, and M. Windsor, "First human use of a new roboticassisted navigation system for small peripheral pulmonary nodules demonstrates good safety profile and high diagnostic yield," *Chest*, vol. 152, no. 4.

[32] N. J. van de Berg, D. J. van Gerwen, J. Dankelman, and J. J. van den Dobbelsteen, "Design choices in needle steeringa review," *IEEE/ASME Transactions on Mechatronics*, vol. 20, no. 5.

[33] C. Gilbert, J. Akulian, R. Ortiz, H. Lee, and L. Yarmus, "Novel bronchoscopic strategies for the diagnosis of peripheral lung lesions: present techniques and future directions," *Radiology*, vol. 19, no. 5.

[34] Y. Wang, W. Li, X. He, G. Li, and L. Xu, "Computed tomographyguided core needle biopsy of lung lesions: Diagnostic yield and correlation between factors and complications," *Oncology Letters*, vol. 7.

[35] D. A. Schreiber, D. B. Shak, A. M. Norbash, and M. C. Yip, "An open-source 7-axis robotic platform to enable dexterous procedures within ct scanners," 2019.

[36] D. A. Schreiber, H.Jiang, G. Li, J. Yu, Z. Yu, R. Zhu, A. M. Norbash, and M. C. Yip, "Crane: A highly dexterous needle placement robot for evaluation of interventional radiology procedures," 2019.

[37] E. Rohmer, S. P. Singh, and M. Freese, "V-rep: A versatile and scalable robot simulation framework," 2013.

[38] S. James, M. Freese, and A. J. Davison, "Pyrep: Bringing v-rep to deep robot learning," 2019.

[39] A. Balestrino, G. D. Maria, and L. Sciavicco, "Robust control of robotic manipulators," 1984, pp. 2435–2440.

[40] W. A. Wolovich and H. Elliot, "A computational technique for inverse kinematics," 1984, pp. 1359–1363.

[41] D. E. Whitney, "Resolved motion rate control of manipulators and human prostheses," *IEEE Transactions on Man-Machine Systems*, vol. 10.

[42] C. W. Wampler, "Manipulator inverse kinematic solutions based on vector formulations and damped least squares methods," *IEEE Transactions on Systems, Man, and Cybernetics*, vol. 16.

[43] Y. Nakamura and H. Hanafusa, "Inverse kinematics solutions with singularity robustness for robot manipulator control," *Journal of Dynamic Systems, Measurement, and Control*, vol. 108.

[44] L.-C. T. Wang and C. C. Chen, "A combined optimization method for solving the inverse kinematics problem of mechanical manipulators," *IEEE Transactions on Robotics and Automation*, vol. 7.

[45] J. Zhao and N. I. Badler, "Inverse kinematics positioning using nonlinear programming for highly articulated figures," *ACM Transactions on Graphics*, vol. 13.

[46] R. Grzeszczuk and D. Terzopoulos, "Automated learning of muscleactuated locomotion through control abstraction," 1995, pp. 63–70.

[47] G. G. Lendaris, K. Mathia, and R. Sacks, "Linear hopfield networks and constrained optimization," *IEEE Transactions on Systems, Man, and Cybernetics — Part B: Cybernetics*, vol. 29.

[48] L. Sciavicco and B. Siciliano, "A solution algorithm to the inverse kinematic problem for redundant manipulators," *IEEE Journal on Robotics and Automation*, vol. 4, no. 4, pp. 403–410, 1988.

[49] A. A. Maciejewski and C. A. Klein, "Obstacle avoidance for kinematically redundant manipulators in dynamically varying environments," *Int. J. Robotics Res.*, vol. 4, no. 3.

[50] M. Freese, F. Ozaki, and N. Matsuhira, "Collision detection, distance calculation and proximity sensor simulation using oriented bounding box trees," 2004, pp. 13–18.

[51] T. Yoshikawa, "Manipulability of robotic mechanisms," *The International Journal of Robotics Research*, vol. 4, no. 2.